MATERIALS SCIENCE

What is the origin of macroscopic friction?

H. Sakuma[1]*, K. Kawai[2], I. Katayama[3], S. Suehara[1]

What is the origin of molecular friction, and how can macroscopic friction be explained in terms of molecular friction? To elucidate the origins of molecular and macroscopic friction, we conducted density functional theory calculations and double-direct shear tests at normal stresses ranging from 5 to 60 MPa for mica surfaces. Frictional forces between mica surfaces were theoretically predicted to oscillate periodically every 30° of sliding direction, in agreement with previous experimental findings. This result affirms that the potential energy roughness of mica under sliding is the origin of molecular friction, which depends on the normal stress and sliding direction. The discovered mechanism of molecular friction can quantitatively explain experimentally observed macroscopic friction of mica when the presence of wear particles is taken into consideration.

INTRODUCTION

Macroscopic frictional forces are proportional to applied loads according to Amontons's law (1), which has been explained based on a combination of two linear relationships: (i) between the real area of contact A_{real} and the applied load L, $A_{real} \propto L$, and (ii) between the frictional force F_f and the real area of contact, $F_f \propto A_{real}$. The first relationship between A_{real} and L is controversial at molecular-scale friction (2, 3). The second linear relationship, $F_f \propto A_{real}$, may be applicable at the molecular scale (4), although the mechanism responsible for such a molecular-scale relationship is unclear. The origin of the frictional force has been considered to be the adhesion at contact (5, 6); however, no correlation has been confirmed between the frictional strength and the adhesive force of sheet-structure minerals (7). The observation of an anisotropic frictional force with respect to the crystallographic sliding direction for copper (8) and mica surfaces (9) implies that the scalar adhesive force cannot explain such anisotropic sliding friction. Hence, there is a need to know both the origin of molecular-scale friction and the relationship between molecular-scale friction and macroscopic friction.

Here, we report the results of studies of molecular-scale and macroscopic frictions of mica using experimental double-direct shear tests and first-principles electronic calculations based on density functional theory (DFT). The characteristics of the potential energy surfaces (PESs) of sliding planes may be critical for understanding molecular friction (10). The conceptual Prandtl-Tomlinson model (11, 12) was used to convert the obtained PES to frictional forces. In the experimental double-direct shear test, macroscopic normal stresses of 5 to 60 MPa were applied to mica sheets; these normal stresses transmit force at a real area of contact on the order of gigapascal (13). Comparison of these experimental results with theoretical calculations revealed how molecular friction could explain macroscopic friction.

RESULTS

Muscovite mica [$KAl_2(OH)_2Si_3AlO_{10}$] is a layered mineral structurally composed of an octahedral sheet sandwiched between two tetrahedral sheets. Isomorphous substitution of Al^{3+} for Si^{4+} in tetrahedra generates negative charges on the layer that are compensated for by inter-

layer K^+ ions. We chose six sliding paths (1 to 6 in Fig. 1) that included the major directions in the cleavage planes corresponding to the crystallographic symmetry. The PES in response to the applied load was calculated by defining the interlayer potential energy (fig. S1) and work performed against the applied load (10).

The calculated potential energy changed along sliding path 1 at several normal stresses from 0.0 to 5.3 GPa and peaked at $D = 2.3$ Å, the position where the oxygen of tetrahedral sheet is located above the interlayer K^+ ion (Fig. 1C). There was a similar maximum of the calculated potential energy along all six paths. The periodicity of the potential energy variations along paths 1, 3, and 5 was short. The analogous periodicity along paths 2, 4, and 6 was long, and the potential energy was comparatively high. The potential energies along paths 3, 5, and 6 where the sliding ended were not zero because of the effect of the partial substitution of Al^{3+} for Si^{4+} in the tetrahedral sites; the lengths of these paths therefore corresponded to half of one period.

The shear stress τ can be obtained from the derivative of the PES along the sliding paths. Because the potential energy profiles can be categorized into two groups (paths 1, 3, and 5 versus paths 2, 4, and 6), the shear stresses of paths 1 and 4 were plotted as representatives of these two groups (Fig. 2, A and B, and fig. S2). A positive shear stress corresponds to the stress required to slide the upper layer of mica. It is clear from the areas under the respective curves that this stress was larger for path 1 (Fig. 2A) than for path 4 (Fig. 2B). We describe the average positive shear stress τ as a linear function of the normal stress σ_n ($\tau = \mu\sigma_n + \tau_0$; solid lines in Fig. 2C); here, the parameters μ and τ_0 bear a different meaning from both the analogous parameters in Amontons's law and the measurements of surface forces (4). Because the simulations in this study were conducted with a constant real area of contact, the parameter μ cannot be interpreted by the ratio of shear strength at the real area of contact and the indentation hardness of mica. The values of μ and τ_0 oscillated with a period of 30° in terms of the sliding direction (Fig. 2D and table S1). This periodicity is consistent with the anisotropy of the frictional force between muscovite surfaces in a dry atmosphere (9). The variation of the PES barrier can explain the dependency of τ_0 on the sliding direction. Note that τ_0 does not originate from an adhesive force but rather from the roughness of the PES. Contributions of viscous forces and thermal effects on the friction of mica were negligible, as discussed in the Supplementary Materials.

Double-direct shear tests of the cleavage planes of mica on two sliding planes were performed as in our previous studies (14, 15) (Fig. 3A). The sliding direction <010> was chosen for sliding along

[1]National Institute for Materials Science, 1-1 Namiki, Tsukuba 305-0044, Japan. [2]Department of Earth and Planetary Science, School of Science, The University of Tokyo, Bunkyo, Tokyo, Japan. [3]Department of Earth and Planetary Systems Science, Hiroshima University, Higashi-Hiroshima, Hiroshima, Japan.
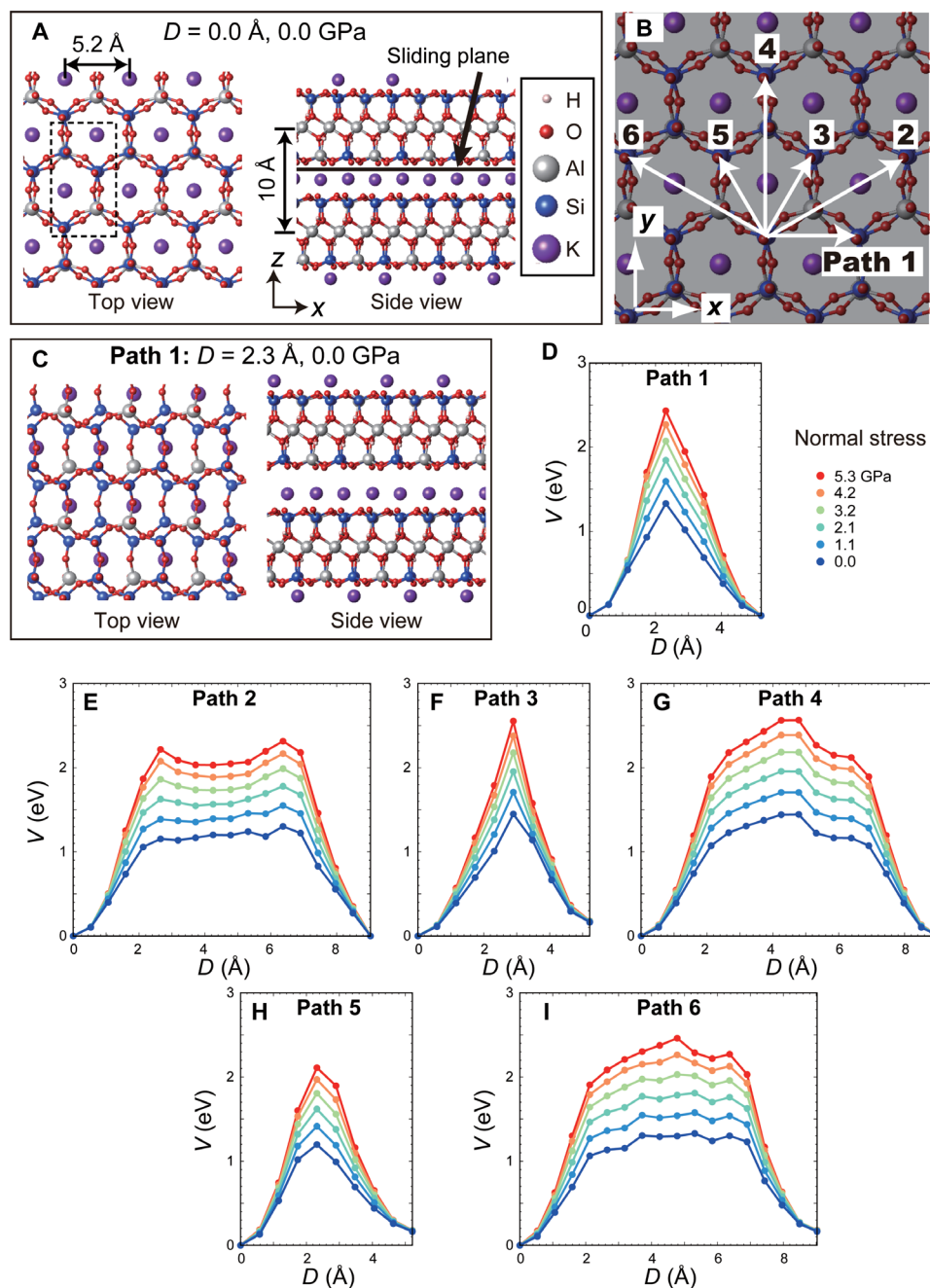*Corresponding author. Email: sakuma.hiroshi@nims.go.jp

Fig. 1. Mica structures, sliding directions, and the potential energy changes along the sliding paths. (**A**) Relaxed structures of the top and side views for D = 0.0 Å under no applied normal stress. The tetrahedral sheets and interlayer potassium ions are shown in the top view. The dashed line indicates the unit area of simulation cell. The cell parameters of the supercell were fixed to a = 5.2026 Å, b = 9.03695 Å, c = 41.41998 Å, α = 90°, β = 95.50°, and γ = 90°. (**B**) Mica structure and the directions of six sliding paths from paths 1 to 6. (**C**) Relaxed structures of the top and side views for D = 2.3 Å under no applied normal stress along path 1. (**D** to **I**) Theoretical change of the potential energy (V) of an upper mica layer relative to a lower layer with distance (D) along six sliding paths. The line plots show potential energy change along the sliding paths, with the applied normal stresses from 0 to 5.3 GPa encoded by colors. The crystal structures were visualized using VESTA software (*25*).

path 4. The friction coefficient deduced by dividing the shear force by the normal force was plotted as a function of shear displacement (Fig. 3B). At the normal stresses below 40 MPa, a plateau, which corresponds to the steady state, is preceded by an asymptotic growth of the friction coefficient. The friction coefficients at steady state were 0.3, 0.28, and 0.25 for normal stresses of 5, 10, and 20 MPa, respectively. At the higher normal stress, the friction coefficient monotonically increases with the shear displacement. The maximum friction coefficients of 0.23 and 0.24 for normal stresses of 40 and 60 MPa, respectively, were chosen for further analysis.
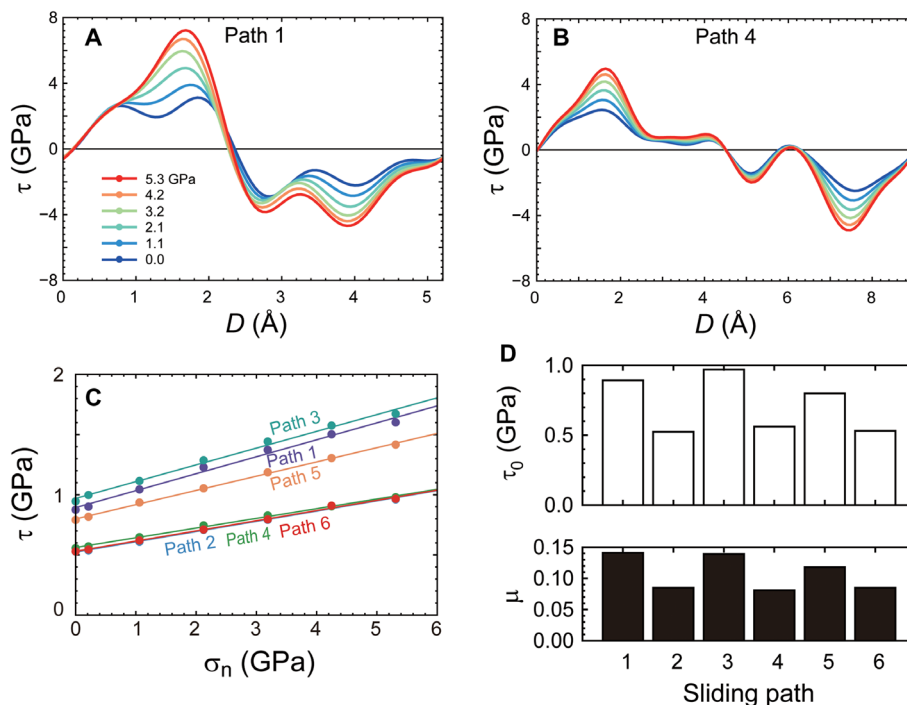
Fig. 2. Shear stresses along sliding paths. Shear stresses along paths 1 (**A**) and 4 (**B**) under applied normal stresses from 0 to 5.3 GPa. (**C**) Average shear stress as a function of the normal stress. Solid lines indicate the results fitted to the linear equation $\tau = \mu\sigma_n + \tau_0$ by a damped least-squares method. (**D**) Fitting parameters of τ_0 and μ of the six sliding paths.
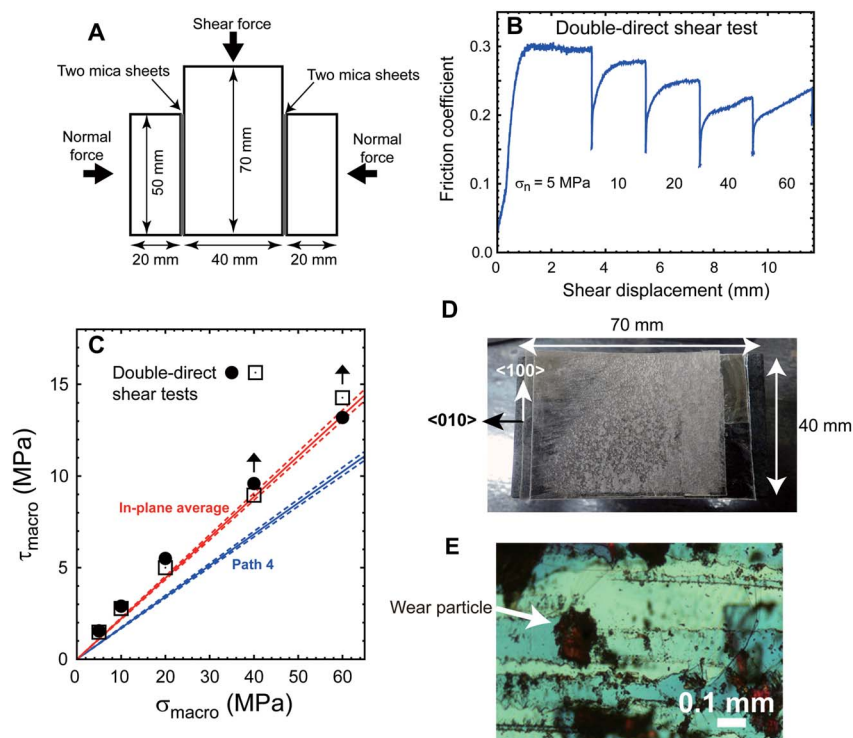

Fig. 3. Shear experiments and a comparison with the theoretical predictions. (**A**) Schematic of the double-direct shear test. Oven-dried mica sheets were embedded between the side and central blocks and placed in a chamber to realize almost 0% of relative humidity by nitrogen atmosphere in the chamber. The depth of all blocks was 40 mm. (**B**) Experimental friction coefficient as a function of shear displacement along the sliding path 4. The initially applied normal stress of 5 MPa was increased to 60 MPa. (**C**) Results of double-direct shear tests compared to those derived from the DFT calculations along path 4 (blue line) and the average of paths 1 to 6 (red line). The dashed lines indicate the SD of hardness measurements. The results of each of two experimental runs are plotted as filled circles or open squares. The arrows indicate that these values should increase at steady state. (**D**) Mica sheets recovered from the double-direct shear tests. White wear particles were observed between the mica sheets. (**E**) Optical image of the wear particles observed with a polarizing microscope.

DISCUSSION

The macroscopic friction of mica was predicted on the basis of the DFT calculations and indentation hardness ($H = 6.27 \pm 0.26$ GPa; see the Supplementary Materials). Macroscopic shear stress τ_{macro} can be calculated as a function of normal stress σ_{macro} as follows: $\tau_{macro} = (\mu + \tau_0/H) \sigma_{macro}$. The DFT-predicted values for the direction 4 were smaller than those obtained experimentally (Fig. 3C). The indication is that molecular-scale friction cannot simply scale up to macroscopic friction. In the double-direct shear test, we observed wear particles on the recovered mica sheets (Fig. 3, D and E). Such wear inevitably occurs when shearing molecularly smooth mica surfaces during measurements of surface forces (4). Wear particles of mica would have a plate-like morphology reflecting their crystal structure. We assumed that such wear particles were stable if the basal plane was parallel to the surface of the mica sheets. In this case, the major sliding plane of the wear particles and mica sheets would be parallel to the basal plane. However, coincidental rotation of the wear particles would randomize the sliding direction of the basal planes. Therefore, the frictional force between wear particles and mica surfaces should be averaged over sliding paths. The shear stress predicted by this in-plane averaging was consistent with the experimental results (Fig. 3C). A small underestimation of the shear stress in the DFT calculations implies the presence of the additional frictional mechanisms such as frictions among various crystal planes, delamination and fracture of mica surfaces, and wear particles.

Our study demonstrated that the molecular friction between mica surfaces can be explained by the roughness of PES. This molecular friction can be applied to the macroscopic friction by considering the presence of wear particles. This indicates that the PES for various sliding planes is useful for predicting the macroscopic friction. The roughness of PES should be varied, depending on the interaction between adjacent layers of sheet-structure minerals; therefore, the difference of PES among sheet-structure minerals can be a clue for understanding the difference of friction coefficients that are critical for the strength of natural faults (16–18).

MATERIALS AND METHODS
DFT calculations

The DFT calculations were conducted under the generalized gradient approximation of Perdew-Burke-Ernzerhof (19) for the exchange and correlation functional. Dispersion force was corrected semiempirically by the DFT-D2 method (20). The Garrity-Bennett-Rabe-Vanderbilt pseudopotentials (21) were used for describing the valence electrons of atoms; the cutoff pseudopotential energies of wave functions and electron density were fixed at 544 and 4354 eV, respectively, by considering the convergence of total energy and lattice constants of muscovite. K-point sampling by the Monkhorst-Pack method (22) was used, and the number of meshes was fixed at $4 \times 2 \times 1$. These methods were successfully applied for the calculations of the interlayer bonding energy of mica (7). The relaxation of atomic configurations was performed for the initial configurations obtained by translating the upper muscovite layer and fixing the lower muscovite layer and all interlayer K^+ ions. Relaxation criteria of force ($<2.57 \times 10^{-2}$ eV/nm) and total energy ($<1.36 \times 10^{-5}$ eV) convergences were used. All calculations were conducted using QUANTUM ESPRESSO (23).

Analysis of molecular friction

The friction force was calculated from the PES, as in a previous study (10). The sliding plane was chosen to be parallel to the (001) plane of the

muscovite surface and located in the interlayer space between $(Si_3Al)O_4$ tetrahedral sheets. The interlayer potential energy E_{IL} between two mica layers was defined as follows

$$E_{IL}(D, z) = E_{2layer}(D, z) - 2E_{1layer} \quad (1)$$

Here, D is the position along the sliding path, z is the interlayer distance, and $E_{2\,layer}$ and $E_{1\,layer}$ are the total energy of two layers and a single layer placed in the supercell, respectively. If the compressional external load f_{ext} is applied on these layers, the interlayer distance z decreases, and the value of interlayer distance z is defined by the distance where the gradient of E_{IL} is equal to f_{ext} as follows

$$f_{ext} = -\frac{\partial E_{IL}(D, z)}{\partial z} \quad (2)$$

The normalized potential energy $V(D, f_{ext})$ was calculated as a function of D and f_{ext} as follows

$$V(D, f_{ext}) = E_{IL}(D, z(D, f_{ext})) + f_{ext}z(D, f_{ext}) - V_0(D_0, f_{ext}) \quad (3)$$

Here, the first term on the right side is the interlayer potential energy under the applied load, the second term is the work by the applied load, and the third term is the minimum potential energy at position D_0 along the sliding path under the applied load. The frictional force $f_{friction}$ (D, f_{ext}) was defined by the derivative with respect to D of the potential energy as follows

$$f_{friction}(D, f_{ext}) = \frac{\partial V(D, f_{ext})}{\partial D} \quad (4)$$

The steady-state friction force f_{shear} was written as

$$f_{shear} = \frac{1}{\Delta D} \int_0^{\Delta D} f dD \quad (5a)$$

$$\begin{cases} f = f_{friction}(D, f_{ext}) (f_{friction} > 0) \\ f = 0 (f_{friction} \leq 0) \end{cases} \quad (5b)$$

on the assumption that the work by negative frictional force was dissipated via surface phonons. Here, ΔD is the cycle of potential energy along the sliding path. The normal and shear stresses were defined by $\sigma_n = f_{ext}/A_r$ and $\tau = f_{shear}/A_r$, respectively. Here, A_r is the area of contact.

Double-direct shear test

High-quality muscovite sheet $[K_{0.92}Na_{0.09}(Al_{1.78}Fe^{3+}_{0.12}Mg_{0.09}Ti_{0.02})$ $(Si_{3.06}Al_{0.94})O_{10}(OH)_{1.96}F_{0.04}]$ was cut into rectangular solids 50 mm × 40 mm in area and 0.2 to 0.4 mm in thickness. Two cleaved sheets were rinsed in distilled water and dried in a vacuum oven at 100°C for 12 hours. The two sheets were each embedded in a gabbro block just before the shear measurements. The blocks were immediately placed into a humidity-controlled chamber fed with dry nitrogen gas, and a normal force of 1 kN was applied. The lattice misorientation angle defining the crystallographic orientation between the two mica sheets was fixed at 0°. The sliding direction was set parallel to path 4,

as confirmed by polarizing microscopy and x-ray diffraction analysis. The shear stress was measured for normal stresses of 5, 10, 20, 40, and 60 MPa as a function of shear displacement at the shear velocity of 3.0 μm s^{-1}.

Nanoindentation test

Nanoindentation of the two cleaved muscovite mica surfaces was tested with a TI 950 TriboIndenter nanoindenter (Hysitron Inc.) with a diamond Berkovich indenter (TI-0039). The penetration hardness H was obtained from the contact area of the tip, A_i, and the maximum load, P_{max}, as follows

$$H = \frac{P_{max}}{A_i} \qquad (6)$$

A_i was calibrated on a fused quartz surface before the measurements by using a standard method (24) as follows

$$A_i = 30.26 h_c^2 + 1216.83 h_c \qquad (7a)$$

$$h_c = h_{max} - \varepsilon \frac{P_{max}}{S_i} \qquad (7b)$$

Here, h_{max} is the maximum penetration depth, ε is the geometric parameter of the tip (0.75), and S_i is the stiffness measured by the gradient of unloading curve. The indentation test was conducted at nine different points on each mica surface. The distances between the points were sufficient to avoid deformation at adjacent points that would have affected the results.

SUPPLEMENTARY MATERIALS

Supplementary material for this article is available at http://advances.sciencemag.org/cgi/content/full/4/12/eaav2268/DC1

Supplementary Text

Fig. S1. Interlayer potential energy E_{IL} along six sliding paths.

Fig. S2. Shear stresses (τ) along six sliding paths obtained from the derivative with respect to distance of the potential energy curves shown in Fig. 1.

Fig. S3. A representative nanoindentation profile of a mica cleavage plane.

Table S1. The list of best-fit parameters of the average shear stress.

References (26–28)

REFERENCES AND NOTES

1. M. Amontons, De la resistance cause'e dans les machines. Hist. Mém Acad. R. Sci., 206–223 (1699).
2. Y. Mo, K. T. Turner, I. Szlufarska, Friction laws at the nanoscale. Nature 457, 1116–1119 (2009).
3. A. Berman, C. Drummond, J. Israelachvili, Amontons' law at the molecular level. Tribol. Lett. 4, 95–101 (1998).
4. A. M. Homola, J. N. Israelachvili, P. M. Mcguiggan, M. L. Gee, Fundamental experimental studies in tribology: The transition from "interfacial" friction of undamaged molecularly smooth surfaces to "normal" friction with wear. Wear 136, 65–83 (1990).
5. F. P. Bowden, D. Tabor, The Friction and Lubrication of Solids (Oxford Univ. Press, 2008).
6. D. E. Moore, D. A. Lockner, Crystallographic controls on the frictional behavior of dry and water-saturated sheet structure minerals. J. Geophys. Res. 109, B03401 (2004).
7. H. Sakuma, S. Suehara, Interlayer bonding energy of layered minerals: Implication for the relationship with friction coefficient. J. Geophys. Res. Solid Earth 120, 2212–2219 (2015).
8. Y. Tsuya, The anisotropy of the coefficient of friction and plastic deformation in copper single crystals. Wear 14, 309–322 (1969).
9. M. Hirano, K. Shinjo, R. Kaneko, Y. Murata, Anisotropy of frictional forces in muscovite mica. Phys. Rev. Lett. 67, 2642–2645 (1991).
10. W. Zhong, D. Tománek, First-principles theory of atomic-scale friction. Phys. Rev. Lett. 64, 3054–3057 (1990).
11. L. Prandtl, Ein Gedankenmodell zur kinetischen Theorie der festen Körper. ZAMM Z. Angew. Math. Mech. 8, 85–106 (1928).
12. G. A. Tomlinson, A molecular theory of friction. Philos. Mag. J. Sci. 7, 905–939 (1929).
13. J. M. Logan, L. W. Teufel, The effect of normal stress on the real area of contact during frictional sliding in rocks. Pure Appl. Geophys. 124, 471–485 (1986).
14. K. Kawai, H. Sakuma, I. Katayama, K. Tamura, Frictional characteristics of single and polycrystalline muscovite and influence of fluid chemistry. J. Geophys. Res. Solid Earth 120, 6209–6218 (2015).
15. H. Tetsuka, I. Katayama, H. Sakuma, K. Tamura, Effects of humidity and interlayer cations on the frictional strength of montmorillonite. Earth Planets Space 70, 56 (2018).
16. D. A. Lockner, C. Morrow, D. Moore, S. Hickman, Low strength of deep San Andreas fault gouge from SAFOD core. Nature 472, 82–85 (2011).
17. B. M. Carpenter, C. Marone, D. M. Saffer, Weakness of the San Andreas Fault revealed by samples from the active fault zone. Nat. Geosci. 4, 251–254 (2011).
18. I. Katayama, T. Kubo, H. Sakuma, K. Kawai, Can clay minerals account for the behavior of non-asperity on the subducting plate interface? Prog. Earth Planet Sci. 2, 30 (2015).
19. J. P. Perdew, K. Burke, M. Ernzerhof, Generalized gradient approximation made simple. Phys. Rev. Lett. 77, 3865–3868 (1996).
20. S. Grimme, Semiempirical GGA-type density functional constructed with a long-range dispersion correction. J. Comput. Chem. 27, 1787–1799 (2006).
21. K. F. Garrity, J. W. Bennett, K. M. Rabe, D. Vanderbilt, Pseudopotentials for high-throughput DFT calculations. Comput. Mater. Sci. 81, 446–452 (2014).
22. H. J. Monkhorst, J. D. Pack, Special points for Brillouin-zone integrations. Phys. Rev. B 13, 5188–5192 (1976).
23. P. Giannozzi, S. Baroni, N. Bonini, M. Calandra, R. Car, C. Cavazzoni, D. Ceresoli, G. L. Chiarotti, M. Cococcioni, I. Dabo, A. Dal Corso, S. de Gironcoli, S. Fabris, G. Fratesi, R. Gebauer, U. Gerstmann, C. Gougoussis, A. Kokalj, M. Lazzeri, L. Martin-Samos, N. Marzari, F. Mauri, R. Mazzarello, S. Paolini, A. Pasquarello, L. Paulatto, C. Sbraccia, S. Scandolo, G. Sclauzero, A. P. Seitsonen, A. Smogunov, P. Umari, R. M. Wentzcovitch, QUANTUM ESPRESSO: A modular and open-source software project for quantum simulations of materials. J. Phys. Condens. Matter. 21, 395502 (2009).
24. W. C. Oliver, G. M. Pharr, An improved technique for determining hardness and elastic modulus using load and displacement sensing indentation experiments. J. Mater. Res. 7, 1564–1583 (1992).
25. K. Momma, F. Izumi, VESTA 3 for three-dimensional visualization of crystal, volumetric and morphology data. J. Appl. Crystallogr. 44, 1272–1276 (2011).
26. C. D. Dushkin, K. Kurihara, A resonance shear force rheometer modeled as simple oscillating circuit. Rev. Sci. Instrum. 69, 2095–2104 (1998).
27. Y. Sang, M. Dubé, M. Grant, Thermal effects on atomic friction. Phys. Rev. Lett. 87, 174301 (2001).
28. J. H. Dieterich, B. D. Kilgore, Imaging surface contacts: Power law contact distributions and contact stresses in quartz, calcite, glass and acrylic plastic. Tectonophysics 256, 219–239 (1996).

What is the origin of macroscopic friction?

H. Sakuma, K. Kawai, I. Katayama and S. Suehara

ARTICLE TOOLS	http://advances.sciencemag.org/content/4/12/eaav2268
SUPPLEMENTARY MATERIALS	http://advances.sciencemag.org/content/suppl/2018/12/17/4.12.eaav2268.DC1
REFERENCES	This article cites 26 articles, 0 of which you can access for free http://advances.sciencemag.org/content/4/12/eaav2268#BIBL
PERMISSIONS	http://www.sciencemag.org/help/reprints-and-permissions

Use of this article is subject to the Terms of Service